Chemical Science

ROYAL SOCIETY OF CHEMISTRY

EDGE ARTICLE

View Article Online
View Journal | View Issue



Cite this: *Chem. Sci.*, 2022, **13**, 7509

All publication charges for this article have been paid for by the Royal Society of Chemistry



# Preparation of trimetallic electrocatalysts by one-step co-electrodeposition and efficient $CO_2$ reduction to ethylene†

Shuaiqiang Jia, [ac] Qinggong Zhu, [*b] Haihong Wu, [*ac] Shitao Han, [ac] Mengen Chu, [ac] Jianxin Zhai, [ac] Xueqing Xing, [d] Wei Xia, [ac] Mingyuan He [ac] and Buxing Han [*abc]

Use of multi-metallic catalysts to enhance reactions is an interesting research area, which has attracted much attention. In this work, we carried out the first work to prepare trimetallic electrocatalysts by a one-step co-electrodeposition process. A series of Cu–X–Y (X and Y denote different metals) catalysts were fabricated using this method. It was found that $Cu_{10}La_1Cs_1$ (the content ratio of $Cu^{2+}$, $La^{3+}$, and $Cs^+$ in the electrolyte is 10 : 1 : 1 in the deposition process), which had an elemental composition of $Cu_{10}La_{0.16}Cs_{0.14}$ in the catalyst, formed a composite structure on three dimensional (3D) carbon paper (CP), which showed outstanding performance for $CO_2$ electroreduction reaction ($CO_2RR$) to produce ethylene ($C_2H_4$). The faradaic efficiency (FE) of $C_2H_4$ could reach 56.9% with a current density of 37.4 mA $cm^{-2}$ in an H-type cell, and the partial current density of $C_2H_4$ was among the highest ones up to date, including those over the catalysts consisting of Cu and noble metals. Moreover, the FE of $C_{2+}$ products ($C_2H_4$, ethanol, and propanol) over the $Cu_{10}La_1Cs_1$ catalyst in a flow cell reached 70.5% with a high current density of 486 mA $cm^{-2}$. Experimental and theoretical studies suggested that the doping of La and Cs into Cu could efficiently enhance the reaction efficiency *via* a combination of different effects, such as defects, change of electronic structure, and enhanced charge transfer rate. This work provides a simple method to prepare multi-metallic catalysts and demonstrates a successful example for highly efficient $CO_2RR$ using non-noble metals.

Received 14th December 2021
Accepted 7th June 2022

DOI: 10.1039/d1sc06964k

rsc.li/chemical-science

## Introduction

Electrocatalytic reduction of $CO_2$ into value-added chemicals is emerging as a sustainable carbon-neutral approach to recycle $CO_2$ and store intermittent renewable electricity.[1,2] As an important $C_2$ product of $CO_2RR$, $C_2H_4$ is compatible with existing industrial infrastructure and can be used to produce a wide range of chemicals, particularly plastics and polymers.[3–6] At present, $C_2H_4$ is mainly manufactured by thermal cracking of crude oil-derived naphtha and hydrogenation of CO *via* Fischer–Tropsch synthesis, and the selectivity is generally not high.[7–9] Although electrocatalytic reduction of $CO_2$ provides a straightforward way for $C_2H_4$ production, achieving high selectivity of $C_2H_4$ and high current density remains a challenge. To date, Cu-based catalyst is uniquely active to promote C–C coupling and yield $C_{2+}$ products, but a single Cu catalyst still suffers from unsatisfied selectivity toward specified hydrocarbons.[10–12] For that, several strategies have been proposed in constructing Cu-based catalysts, including surface reconstruction,[13–15] hybridization,[9,16] crystalline faceting,[17,18] nano/meso-structuring,[19,20] defect engineering,[21,22] or creating multi-metallic structural motifs,[23–25] *etc.*

Constructing multi-metallic structures has attracted considerable interest since it can create abundant defects to enhance the $CO_2$-to-$C_{2+}$ products activity through optimizing the binding energy among reactants, intermediates, and products with the multi-metallic surface at the nanoscale.[26,27] So far, the most active doping metallic elements are still noble metals, because the presence of noble metals can easily modulate strains and lattice disorders of the Cu phase, and precisely steer the two pivotal steps towards $C_2H_4$ formation, including *CO formation and C–C coupling.[28,29] Non-noble metal elements, however, still suffer from low to modest activity. Therefore, the

[a]*Shanghai Key Laboratory of Green Chemistry and Chemical Processes, School of Chemistry and Molecular Engineering, East China Normal University, Shanghai 200062, China. E-mail: hhwu@chem.ecnu.edu.cn; hanbx@iccas.ac.cn*

[b]*Beijing National Laboratory for Molecular Sciences, CAS Key Laboratory of Colloid and Interface and Thermodynamics, CAS Research/Education Center for Excellence in Molecular Sciences, Institute of Chemistry, Chinese Academy of Sciences, Beijing 100190, China. E-mail: qgzhu@iccas.ac.cn*

[c]*Institute of Eco-Chongming, 20 Cuiniao Road, ChenjiaTown, Chongming District, Shanghai 202162, China*

[d]*Beijing Synchrotron Radiation Facility, Institute of High Energy Physics, Chinese Academy of Sciences, Beijing 100049, China*

† Electronic supplementary information (ESI) available. See https://doi.org/10.1039/d1sc06964k

attempts made to conduct efficient $CO_2$-to-$C_2H_4$ electrocatalysts rely mostly on bimetallic materials involving noble metals, such as Cu–Au, Cu–Ag, Cu–Pd, *etc.*[30–35] Unlike the bimetallic catalysts, integrating trimetallic nanostructures manifest great prospects in efficient $CO_2$RR to $C_{2+}$ products.[36,37] To date, however, only Cu–Au/Ag nanoframes have shown promise for enhancing the efficiency of $C_2H_4$ production, in which the CO generation was promoted by the alloyed Ag/Au and the C–C coupling was facilitated by the highly strained and positively charged Cu domains (ESI Table S1†).[36] However, conventional trimetallic catalysts still require the participation of noble metals and a complicated preparation process. Therefore, the rational design of non-noble trimetallic electrocatalysts with a facial synthesis strategy is highly desired for the practical deployment of electrochemical $CO_2$RR.

Herein, we report a one-step strategy to synthesize trimetallic catalysts by co-electrodeposition. A series of trimetallic catalysts Cu–X–Y (X, Y = La, Cs, Zn, Co, Ag, Au) have been developed for $CO_2$RR. It was discovered that co-electrodeposition can form a trimetallic composite structure that grown on CP. The presence of non-noble metals La and Cs could create abundant defects and modulate the electronic structure of the Cu phase, offering substantial active sites to stabilize the intermediates and promote C–C coupling to product $C_2H_4$. The as-synthesized trimetallic catalysts also provided large electrochemical surface area and facilitated charge transfer, which enhanced the reaction rate. The high $CO_2$ electrocatalytic performance was demonstrated over $Cu_{10}La_1Cs_1$ (the concentrations ratio of $Cu^{2+}$, $La^{3+}$, and $Cs^+$ in the electrolyte is 10 : 1 : 1 in the deposition process) with up to 56.9% $C_2H_4$ selectivity with a current density of 37.4 mA $cm^{-2}$ in an H-type cell, and a total $C_{2+}$ selectivity of 70.5% with a current density of 485.5 mA $cm^{-2}$ in a flow cell, respectively.

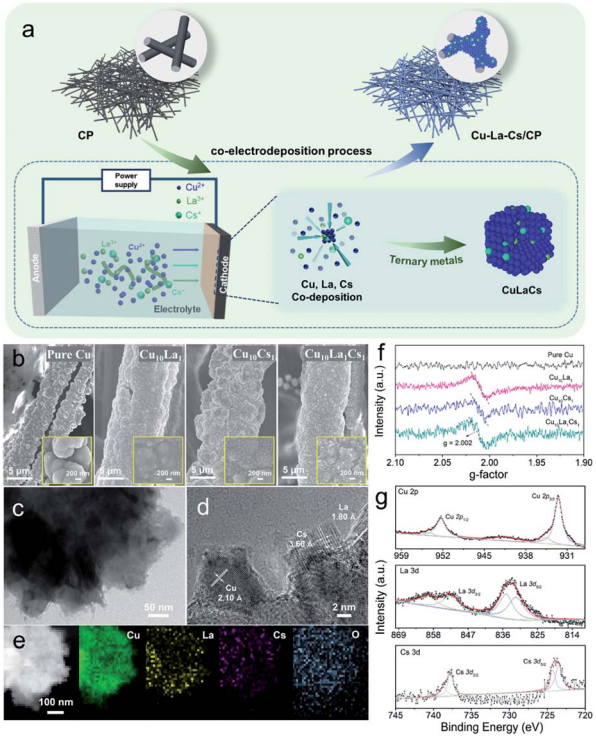


Fig. 1 (a) Schematic illustration of the process to prepare pure Cu, bimetallic Cu–La or Cu–Cs, and trimetallic Cu–La–Cs catalysts; structural characterization of Cu–La–Cs catalysts: (b) SEM images of pure Cu, $Cu_{10}La_1$, $Cu_{10}Cs_1$, and $Cu_{10}La_1Cs_1$ catalysts on a fiber of CP obtained after electrodeposition at a constant voltage of 4 V for 2 min (inset: high-magnification); (c, d) TEM images and HR-TEM image of $Cu_{10}La_1Cs_1$ catalyst; and (e) elemental mappings images of $Cu_{10}La_1Cs_1$ catalysts; (f) EPR spectra of pure Cu, $Cu_{10}La_1$, $Cu_{10}Cs_1$, and $Cu_{10}La_1Cs_1$ catalysts at room temperature; (g) XPS spectra of Cu 2p spectra, La 3d spectra, and Cs 3d spectra in $Cu_{10}La_1Cs_1$ catalyst.

## Results and discussion

To understand how trimetallic cooperation might tune the electrocatalytic activity, we prepared a group of trimetallic electrocatalysts (Cu–X–Y; X, Y = La, Cs, Zn, Co, Ag, Au). The non-noble trimetallic catalysts were grown on three-dimension CP (ESI Fig. S1†) through a one-step co-electroplating process, which was illustrated in Fig. 1a using trimetallic Cu–La–Cs as a representative example. Typically, a piece of CP with a geometric area of 1 $cm^2$ and a Pt gauze were used for the cathodic and anodic electrodes with a gap of 1 cm, and the electrochemical experiments could be controlled by a DC Power supply. Before all the experiments, the CP was ultrasonically cleaned with acetone, ethanol, and deionized water. For the $Cu_{10}La_1Cs_1$ electrode, the electrodeposition was carried out cathodically using a 50 mL solution of $H_2SO_4$ (10 mM), Cu(II) gluconate (100 mM), La(III) acetate (10 mM), Cs(I) acetate (10 mM), and 4-aminopyridine (10 mM). The deposition was carried out at a constant voltage of 4 V for 2 min. When the molar ratio of Cu(II), La(III), and Cs(I) in the electrolyte was 10 : 1 : 1, the as-synthesized catalyst was denoted as $Cu_{10}La_1Cs_1$ with a total loading of 1.33 mg metals on 1.0 $cm^{-2}$ CP (Table S2†), and the contents of Cu, La, and Cs in $Cu_{10}La_1Cs_1$ were 93.92 wt%, 3.31 wt%, and 2.77 wt% (Table S3†), respectively, as determined by inductively coupled plasma optical emission spectroscopy (ICP-OES).

The scanning electron microscopy (SEM) images reveal that trimetallic $Cu_{10}La_1Cs_1$ film grew uniformly on the fiber of the 3D CP substrate (Fig. 1b). Inset in Fig. 1b shows that the Cu, $Cu_{10}La_1$, $Cu_{10}Cs_1$, and $Cu_{10}La_1Cs_1$ catalyst films had a rough surface. Besides, transmission electron microscopy (TEM) images confirm the formation of $Cu_{10}La_1Cs_1$ trimetallic nanostructure, which was different from the pure Cu structure (Fig. 1c, d and S2†).

The high-resolution TEM (HR-TEM) image exhibit that the interplanar spacing was 2.10 Å, corresponding to the d spacing of (111) plane of Cu (Fig. 1d and S3a, b†), which is similar to pure Cu catalyst (Fig. S2†). In addition, the observed fringes with an interlayer spacing of 3.60 Å and 1.80 Å correspond to the (012) plane of $Cs_2O$ (JCPDS card no. 09-0104), and the (211) plane of $La_2O_3$ (JCPDS card no. 40-1284) (Fig. 1d and S3c–f†). The elemental distribution mapping (EDS) further confirmed the uniform dispersion of Cu, La, and Cs species in the trimetallic $Cu_{10}La_1Cs_1$ catalysts (Fig. 1e). The abundant vacancies and lattice disorder could also be observed in $Cu_{10}La_1Cs_1$

(Fig. S4 and S5†), which indicates that defect-rich nanostructure existed in the catalyst. Such defects result in high exposure of coordination-unsaturated Cu sites, which may change the electronic structure of Cu and influence its catalytic performance.[38,39] The electron paramagnetic resonance (EPR) spectra of different samples were collected at room temperature (Fig. 1f). Compared with pure Cu, typical signals for oxygen vacancy appeared at *g*-value of 2.002 for $Cu_{10}La_1$, $Cu_{10}Cs_1$, and $Cu_{10}La_1Cs_1$ catalysts, which indicates that introducing of La or Cs contributes to the formation of defects (Fig. 1f). The oxygen vacancy was also reported to optimize the adsorption energy of reactants on the catalyst surface, which reduces the reaction energy barrier and promotes molecular activation.[40]

The time-dependent X-ray diffraction (XRD) showed the gradual formation of trimetallic $Cu_{10}La_1Cs_1$ catalysts (Fig. S6†). In detail, the representative peaks could be observed at 43.2°, 50.4°, 74.1°, 89.9°, and 37.0°, which can be indexed to the Cu (111), Cu (200), Cu (220), Cu (311), and $Cu_2O$ (111) planes. However, the diffraction peaks of La and Cs were not shown obviously for trimetallic $Cu_{10}La_1Cs_1$, because their amounts were below the XRD detection threshold. The X-ray photoelectron spectroscopy (XPS) and X-ray absorption spectroscopy (XAS) analyses were performed to further investigate the surface chemical composition and elemental valence states of the catalyst. XPS results showed that the surface of $Cu_{10}La_1Cs_1$ was composed of Cu, La, and Cs species (Fig. 1g and S7†). The peaks at 932.1 eV (Cu $2p_{3/2}$) and 952.0 eV (Cu $2p_{1/2}$) retained the characteristic feature of Cu species, which was further confirmed by the Cu 2p and Auger Cu LMM spectra that the Cu existed as $Cu^0$ and $Cu^+$, and $Cu^0$ was predominant (Fig. S8†). In addition, the XPS spectra could also be fitted to include both La(III) and Cs(I) species, which correspond to peaks at 835.6 eV (La $3d_{5/2}$) and 852.5 eV (La $3d_{3/2}$), 723.9 eV (Cs $3d_{5/2}$) and 743.1 eV (Cs $3d_{3/2}$), respectively (Fig. 1g). These results showed that the Cu, La, and Cs coexisted in the $Cu_{10}La_1Cs_1$ catalysts. To further study the electronic structures and chemical bonding of the Cu phase that was influenced by La and Cs atoms, we performed X-ray absorption spectroscopy (XAS) analysis. The Cu K-edge X-ray absorption near-edge spectra (XANES) spectra of $Cu_{10}La_1Cs_1$ with the reference materials indicated that $Cu_{10}La_1Cs_1$ were mainly composed of $Cu^0$ and $Cu^+$. From the XANES spectrum, it is obvious that the dominated Cu–Cu coordination at 2.23 Å existed in the catalyst, which is identical to that of $Cu^0$ (Fig. S9†). This is in good agreement with the XRD and XPS analyses.

The as-synthesized catalysts were firstly tested for $CO_2RR$ in 0.1 M KCl aqueous electrolyte using a typical H-type cell. The low buffering capability of KCl aqueous electrolytes allowed the electrode surface pH to increase to a weakly basic range, which facilitated the formation of $C_2$ products by combining with efficient electrocatalysts.[41,42] In this study, the linear scanning voltammetry (LSV) curves over various catalysts were determined, including pure Cu, bimetallic $Cu_{10}La_1$, $Cu_{10}Cs_1$, and trimetallic $Cu_{10}La_1Cs_1$ catalysts. As shown in Fig. 2a, over $Cu_{10}La_1Cs_1$ catalyst, the current density (*j*) was much higher in $CO_2$-saturated electrolyte than that in $N_2$-saturated electrolyte from −0.5 V to −1.4 V *vs.* RHE, suggesting the reduction of $CO_2$. Moreover, in $CO_2$-saturated electrolyte, the current density over $Cu_{10}La_1Cs_1$ was higher than that over other catalysts. The electrolysis performances at different potentials over various catalysts are displayed in Fig. 2b, c, and S10–S12.† Under the reaction conditions, the gaseous products were mainly composed of $H_2$, CO, $CH_4$, and $C_2H_4$, which were determined using gas chromatography (GC). The liquid products were evaluated by nuclear magnetic resonance (NMR), and only very small amounts of formic acid (<1%) were detected. The content was very low and was not considerable (Fig. S14†). Clearly, $Cu_{10}La_1Cs_1$ had a much higher FE of $C_2H_4$ than other catalysts at all potentials (Fig. 2b). For pure Cu catalyst, the FE of $C_2H_4$ was only 33.0% at −1.2 V *vs.* RHE, which exhibited an inferior catalytic performance compared with other catalysts (Fig. 2b). For bimetallic $Cu_{10}La_1$ and $Cu_{10}Cs_1$, the FE of $C_2H_4$ increased consistently to 43.6% and 42.5% respectively. The FE of $C_2H_4$ over trimetallic $Cu_{10}La_1Cs_1$ catalyst could reach 56.9% with a current density of 37.4 mA $cm^{-2}$ at −1.2 V *vs.* RHE, suggesting a 2.7-fold increase in partial current density, compared to the pure Cu catalyst (Fig. 2b and S10–S12†). We also synthesized trimetallic Cu–La–Cs catalysts with different Cu–La–Cs ratios. Clearly, $Cu_{10}La_1Cs_1$ had the highest catalytic $CO_2RR$ activity toward $C_2H_4$ production (Fig. S13†). Systematic comparisons to state-of-the-art catalysts revealed that the performance of the trimetallic $Cu_{10}La_1Cs_1$ catalyst with rich-defects was one of the best ones in the H-type cell (Table S1†), including those over the catalysts consisting of Cu and noble metals. Long-term electrolysis was also performed to verify the stability of the catalyst. As shown in Fig. 2d, the current density and FE of $C_2H_4$ over $Cu_{10}La_1Cs_1$ were not changed obviously at −1.2 V *vs.* RHE for 5 h, indicating the stability of the catalyst at the $CO_2RR$ condition. After the reaction, the XRD, EPR, and XPS analyses were performed and the results showed that the properties of the catalyst did not change noticeably (Fig. S15–S17†). The EXAFS at the Cu K-edge confirmed a well-retained Cu interaction in samples collected after the $CO_2RR$ test (Fig. S18†). These results also indicated the remarkable stability of the trimetallic $Cu_{10}La_1Cs_1$ catalyst.

In addition, to gauge the benefits of the trimetallic Cu–La–Cs catalyst for high-rate $CO_2RR$, we translated the catalyst to a gas-diffusion environment (Fig. S19†). In this configuration, hydrophobic CP containing carbon black layer acted as a gas diffusion electrode (GDE). When using 1 M KOH as the electrolyte, we found that $Cu_{10}La_1Cs_1$ could maintain $C_{2+}$ selectivity up to 70.5% with a high current density of 485.5 mA $cm^{-2}$ at a low reduction potential of −0.97 V *vs.* RHE. The FE of $C_{2+}$ products were ethylene (42.1%), ethanol (20.8%), and *n*-propanol (7.6%), respectively (Fig. S20†). The configuration also showed a stable potential profile over 5 h without noticeable decay of the current density and $C_{2+}$ product selectivity (Fig. 2e).

Considering the experimental observations above, we think that the excellent performance of the $Cu_{10}La_1Cs_1$ catalyst resulted partially from the synergistic effect of the components in the trimetallic catalyst. We found that the surface roughness of the catalysts changed obviously with the introduction of La and Cs, which is beneficial for the increasing of active sites.[43] The values of electrochemical double-layer capacitance ($C_{dl}$)

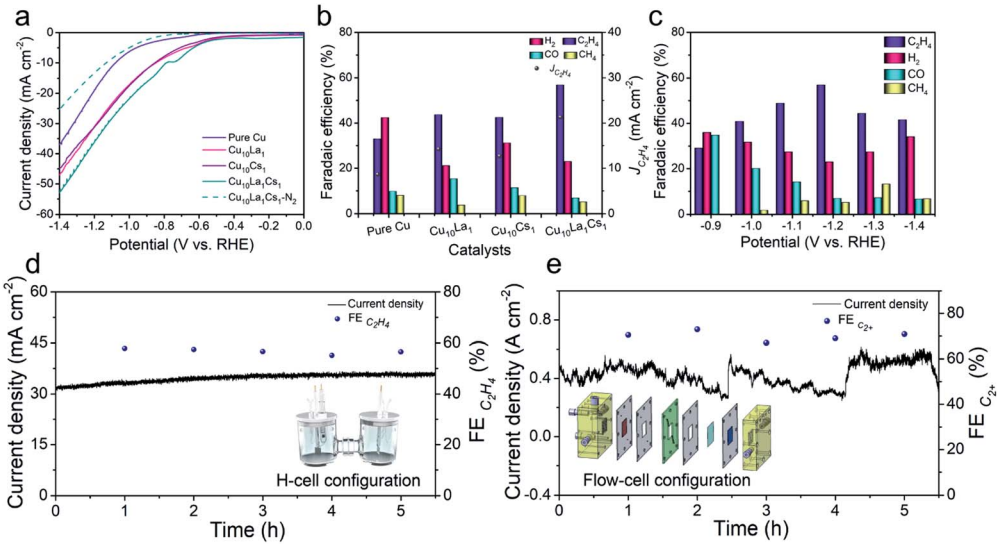


Fig. 2 (a) LSV traces at a scan rate of 50 mV $s^{-1}$ of pure Cu, $Cu_{10}La_1$, $Cu_{10}Cs_1$, and $Cu_{10}La_1Cs_1$ catalysts in $CO_2$-saturated and $N_2$-saturated 0.1 M KCl aqueous electrolyte; (b) the distribution of reduction products and partial current densities for $C_2H_4$ at −1.2 V *vs.* RHE over pure Cu, $Cu_{10}La_1$, $Cu_{10}Cs_1$, and $Cu_{10}La_1Cs_1$ catalysts; (c) the distribution of reduction products at different applied potentials over $Cu_{10}La_1Cs_1$ catalysts; (d) electrochemical stability test of $Cu_{10}La_1Cs_1$ film electrode at −1.2 V *vs.* RHE in an H-type cell; (e) electrochemical stability test of $Cu_{10}La_1Cs_1$ film electrode at −0.97 V *vs.* RHE in a flow cell.

were calculated from cyclic voltammograms (CV) curves (Fig. S21†) to evaluate the electrochemical active surface area (ECSA) of different catalysts. The $C_{dl}$ value of $Cu_{10}La_1Cs_1$ film was calculated to be 4.51 mF $cm^{-2}$, which was obviously higher than that of others (Fig. S22†). It suggested that $Cu_{10}La_1Cs_1$ film with rich-defects could provide more catalytic sites, leading to an increase in reaction rate during the electrocatalytic process. We also used electrochemical impedance spectroscopy (EIS) to study the interfacial properties of the catalysts at an open circuit potential in a $CO_2$-saturated electrolyte (Fig. S23†). The $Cu_{10}La_1Cs_1$ catalyst showed the lowest charge transfer resistance ($R_{ct}$). Therefore, the charge transport is more facile on $Cu_{10}La_1Cs_1$ catalyst, which is favorable to enhance the reaction rate.

To screen the synergistic effect of the components in the trimetallic catalysts, we also prepared a series of $Cu_{10}$–$X_1$–$Y_1$ catalysts using the same method. When the molar ratio of metal ions for Cu, X, and Y in the electrodeposition electrolyte was 10 : 1 : 1, the as-synthesized catalyst was denoted as $Cu_{10}X_1Y_1$. The compositions of these trimetallic catalysts, such as $Cu_{10}Ag_1La_1$, $Cu_{10}Zn_1La_1$, $Cu_{10}Ag_1Cs_1$, $Cu_{10}Zn_1Co_1$, and $Cu_{10}Ag_1Au_1$, were then characterized by ICP-OES, and their element compositions are shown in Tables S3 and S4.† It indicates that the elemental compositions of the trimetallic catalysts varied with different doping components. The $CO_2$RR performance tests of different trimetallic catalysts were conducted, and the results are shown in Fig. 3a. It indicates that the catalytic performances of the metals depended on the metals introduced into Cu. Some metal doping (*e.g.* Ag, Co, and Au) can promote the production of $C_1$ products, while other metal doping (*e.g.* Zn, La, and Cs) can inhibit hydrogen evolution and promote C–C coupling. Among them, $Cu_{10}La_1Cs_1$ yielded the highest FE of $C_2H_4$ and current density. The multi-metallic system could actively generate CO or inhibit cathodic hydrogen evolution reaction during the electrochemical reduction of $CO_2$. The excess amount of CO molecules on the metal surface are expected to migrate to the adjacent Cu surface and then undergo C–C coupling for the formation of $C_2H_4$ products.[6,30,44] The study indicated that the compositions not only significantly influenced the surface morphology of the trimetallic structures (Fig. S24†), but also changed the electronic properties of the catalyst. We then compare the effect of different defect/vacancies on the electronic properties, using $Cu_{10}La_1Cs_1$ and $Cu_{10}Ag_1Au_1$ as a comparing couple. The calculated density of states (DOS) of $Cu_{10}La_1Cs_1$ and $Cu_{10}Ag_1Au_1$ are shown in Fig. 3b. Comparing with the partial density of states (PDOS) for $Cu_d$ orbitals, the electronic environment (the gap states) of the catalyst is constructed jointly by all the metals after doping with La/Cs or Ag/Au, which suggests that doping can significantly promote the electron transfer of the catalyst.[45,46] It suggests that La/Cs doping has a similar effect as Ag/Au doping in regulating the electronic structure of Cu-based catalyst, which is beneficial to the charge transfer for CO dimerization.[47–49] Therefore, we can conclude that the synergistic effect of the components in the trimetallic catalysts can be attributed to the change of different defects/vacancies on the electronic properties and surface structures.

It is worth mentioning that no obvious changes occurred in Cu phase during $CO_2$RR. From the semi-in situ XAS characterization results presented in Fig. 4a–c, we can find that the surface of $Cu_{10}La_1Cs_1$ was still mainly $Cu^0$ sites with the increase of electrolysis time. These data further confirm that the La and Cs components could maintain the chemical state and the local coordination environment of the Cu phase was not changed under reaction conditions. The undercoordinated Cu

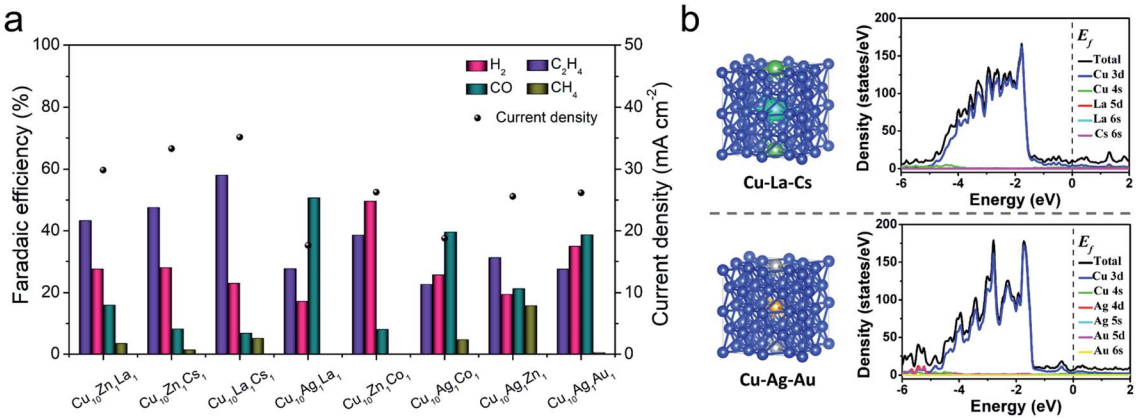


Fig. 3 (a) The distribution of reduction products and current density at −1.2 V *vs.* RHE over different metal catalysts; (b) the structure models and the DOS of $Cu_{10}La_1Cs_1$ and $Cu_{10}Ag_1Au_1$ electrodes. (The atoms in blue, green, viridian, silvery, and brown represent Cu, La, Cs, Ag, and Au, respectively. The doping model shown is Cu 2 × 2 × 2 supercell-based substitution doping).

sites are associated with outstanding C–C coupling.[50–52] We then pursued theoretical insights into the study of the intrinsic property of the catalysts. As depicted in computational structure models in Fig. 4d and S25–S30,† the interactions and electronic structure among Cu, La, and Cs atoms of pure Cu, $Cu_{10}La_1$, $Cu_{10}Cs_1$, and $Cu_{10}La_1Cs_1$ catalysts were different. For $Cu_{10}La_1Cs_1$, the La and Cs atoms tend to delocalize charge by releasing electrons to the Cu atoms, manifesting the electron transfer effect. The optimized adsorption configurations of reaction intermediates on the simulated interface structures are displayed in Fig. S31.† Fig. 4e and f show the *CO and *OCCO adsorption configurations on the four simulated interface structures. We can find that the presence of La and Cs in $Cu_{10}La_1Cs_1$ could effectively adjust the adsorption space position of *CO and *OCCO intermediates to an optimized state, which enables the lowest energy barrier for $CO_2$ transformation to more reduced products with the multi-electron process. This result is obviously different from that over pure Cu catalyst, on which the energy barrier is mainly in the typical two steps of $CO_2$ hydrogenation reduction to generate adsorbed carboxylic acid groups ($CO_2 + H^+ + e^- \rightarrow$ *COOH) and CO molecular copolymerization (*2CO → *OCCO), requiring the high energy barrier.[53] With the introduction of the Cs atom, the energy barrier of these two steps was reduced, and it becomes more

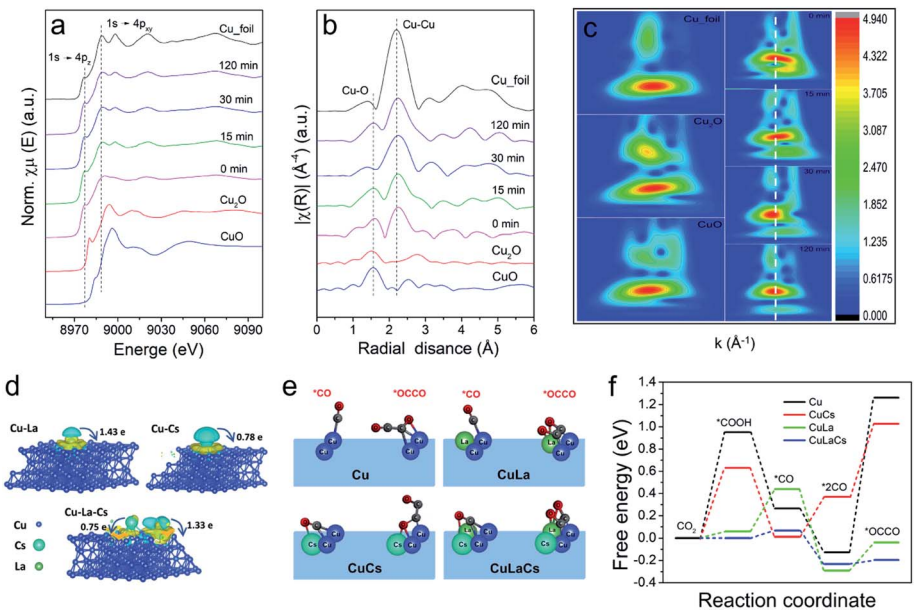


Fig. 4 Semi-in situ XAS characterization and DFT calculations. (a) Normalized Cu K edge XANES spectra of $Cu_{10}La_1Cs_1$ during $CO_2$RR at −1.2 V *vs.* RHE; (b) corresponding $k^3$-weighted FT-EXAFS spectra of $Cu_{10}La_1Cs_1$ during $CO_2$RR at −1.2 V *vs.* RHE; (c) Morlet WT of the $k^3$-weighted EXAFS data for $Cu_{10}La_1Cs_1$ during $CO_2$RR at −1.2 V *vs.* RHE; (d) side views of the charge density difference of $Cu_{10}La_1$, $Cu_{10}Cs_1$, and $Cu_{10}La_1Cs_1$ with an isosurface of $6 \times 10^{-4}$, $2 \times 10^{-3}$ and $2 \times 10^{-3}$ e Å$^{-3}$, respectively. (The charge accumulation is shown as the yellow region, and the charge depletion is shown as the cyan region); (e) the *CO and *OCCO adsorption configurations on pure Cu, $Cu_{10}La_1$, $Cu_{10}Cs_1$, and $Cu_{10}La_1Cs_1$ interface structures; (f) the activation energy barrier of CO dimerization at different models.

noticeable with the further introduction of La atoms. Therefore, we consider that the synergistic effect between Cu, La, and Cs not only reduces the energy barrier for the $CO_2$ hydrogenation reduction to form adsorbed carboxylic acid groups ($CO_2 + H^+ + e^- \rightarrow$ *COOH) and CO molecules (*COOH + $H^+ + e^- + H_2O \rightarrow$ *CO), but also promotes the C–C coupling process for $C_2H_4$ formation (*2CO $\rightarrow$ *OCCO).[54–57] This suggests that the presence of La and Cs favors CO production and leads to higher CO* coverage around the active sites. The increased CO* coverage then improves the dimerization of neighboring *CO intermediates to generate *OCCO rather than desorbed. The above results, taken together, suggest that the synergistic interaction among Cu, La, and Cs can efficiently enhance the $C_2H_4$ selectivity *via* a combination of effects, including defects, change of electronic structure, fast charge transfer rate, and increase of active sites.

## Conclusions

In summary, we find that a trimetallic catalyst prepared *via* a one-step co-electrodeposition strategy can act as a robust electrocatalyst for $CO_2$RR to $C_2H_4$. In particular, over $Cu_{10}La_1Cs_1$ catalyst, the $C_2H_4$ selectivity can reach 56.9% with a current density of 37.4 mA $cm^{-2}$ in an H-type cell, and a total $C_{2+}$ selectivity reaches 70.5% with a current density of 485.5 mA $cm^{-2}$ in a flow cell, respectively. The outstanding electrocatalytic performance of the trimetallic $Cu_{10}La_1Cs_1$ catalyst can be ascribed to the synergistic effect of Cu, La, and Cs. The abundant defects can modulate the electronic structure of the Cu phase, offering substantial potential active sites to stabilize the *CO intermediates and promote C–C coupling to produce $C_2H_4$. The as-synthesized trimetallic catalysts on 3D CP also result in a large electrochemical surface area and fast charge transfer, which enhance the reaction rate. We believe that the methodology to prepare multi-metallic catalysts by co-electrodeposition can also be used to design other efficient catalysts for $CO_2$RR.

## Data availability

The authors declare that all data supporting the findings of this study are available within the paper [and its ESI†].

## Author contributions

S. Q. J., Q. G. Z., H. H. W. and B. X. H. proposed the project, designed the experiments, and wrote the manuscript. S. Q. J. performed the whole experiment. S. T. H., M. E. C., J. X. Z., X. Q. X. and W. X. performed the analysis of experimental data. Q. G. Z., H. H. W., M. Y. H. and B. X. H. co-supervised the whole project. All authors discussed the results and commented on the manuscript.

## Conflicts of interest

The authors declare no competing interests.

## Acknowledgements

The work was supported by the National Key Research and Development Program of China (2020YFA0710201, 2017YFA0403102), the National Natural Science Foundation of China (22022307, 21890761, 22121002). The X-ray Absorption Fine Structure (XAFS) measurements were carried out at the 4B9A beamline of Beijing Synchrotron Radiation Facility (BSRF), China.

## Notes and references

1 X. Chen, J. Chen, N. M. Alghoraibi, D. A. Henckel, R. Zhang, U. O. Nwabara, K. E. Madsen, P. J. A. Kenis, S. C. Zimmerman and A. A. Gewirth, *Nat. Catal.*, 2020, **4**, 20–27.
2 A. Ozden, Y. Wang, F. Li, M. Luo, J. Sisler, A. Thevenon, A. Rosas-Hernández, T. Burdyny, Y. Lum, H. Yadegari, T. Agapie, J. C. Peters, E. H. Sargent and D. Sinton, *Joule*, 2021, **5**, 706–719.
3 X. F. Qiu, H. L. Zhu, J. R. Huang, P. Q. Liao and X. M. Chen, *J. Am. Chem. Soc.*, 2021, **143**, 7242–7246.
4 B. Zhang, J. Zhang, M. Hua, Q. Wan, Z. Su, X. Tan, L. Liu, F. Zhang, G. Chen, D. Tan, X. Cheng, B. Han, L. Zheng and G. Mo, *J. Am. Chem. Soc.*, 2020, **142**, 13606–13613.
5 C. Choi, S. Kwon, T. Cheng, M. Xu, P. Tieu, C. Lee, J. Cai, H. M. Lee, X. Pan, X. Duan, W. A. Goddard and Y. Huang, *Nat. Catal.*, 2020, **3**, 804–812.
6 A. N. Kuhn, H. Zhao, U. O. Nwabara, X. Lu, M. Liu, Y. T. Pan, W. Zhu, P. J. A. Kenis and H. Yang, *Adv. Funct. Mater.*, 2021, **31**, 2101668.
7 R. Shi, Z. Wang, Y. Zhao, G. I. N. Waterhouse, Z. Li, B. Zhang, Z. Sun, C. Xia, H. Wang and T. Zhang, *Nat. Catal.*, 2021, **4**, 565–574.
8 J. Bu, Z. Liu, W. Ma, L. Zhang, T. Wang, H. Zhang, Q. Zhang, X. Feng and J. Zhang, *Nat. Catal.*, 2021, **4**, 557–564.
9 P. Shao, W. Zhou, Q. L. Hong, L. Yi, L. Zheng, W. Wang, H. X. Zhang, H. Zhang and J. Zhang, *Angew. Chem., Int. Ed.*, 2021, **60**, 16687–16692.
10 X. Yuan, S. Chen, D. Cheng, L. Li, W. Zhu, D. Zhong, Z. J. Zhao, J. Li, T. Wang and J. Gong, *Angew. Chem., Int. Ed.*, 2021, **60**, 15344–15347.
11 H. Li, T. Liu, P. Wei, L. Lin, D. Gao, G. Wang and X. Bao, *Angew. Chem., Int. Ed.*, 2021, **60**, 14329–14333.
12 H. S. Jeon, J. Timoshenko, C. Rettenmaier, A. Herzog, A. Yoon, S. W. Chee, S. Oener, U. Hejral, F. T. Haase and B. Roldan Cuenya, *J. Am. Chem. Soc.*, 2021, **143**, 7578–7587.
13 M. G. Kibria, C. T. Dinh, A. Seifitokaldani, P. De Luna, T. Burdyny, R. Quintero-Bermudez, M. B. Ross, O. S. Bushuyev, F. P. Garcia de Arquer, P. Yang, D. Sinton and E. H. Sargent, *Adv. Mater.*, 2018, **30**, 1804867.
14 C. M. Gunathunge, X. Li, J. Li, R. P. Hicks, V. J. Ovalle and M. M. Waegele, *J. Phys. Chem. C*, 2017, **121**, 12337–12344.
15 D. Wakerley, S. Lamaison, F. Ozanam, N. Menguy, D. Mercier, P. Marcus, M. Fontecave and V. Mougel, *Nat. Mater.*, 2019, **18**, 1222–1227.
16 X.-Q. Li, G.-Y. Duan, J.-W. Chen, L.-J. Han, S.-J. Zhang and B.-H. Xu, *Appl. Catal. B Environ.*, 2021, **297**, 120471.

17 F. S. Roberts, K. P. Kuhl and A. Nilsson, *Angew. Chem., Int. Ed.*, 2015, **54**, 5179–5182.
18 W. Luo, X. Nie, M. J. Janik and A. Asthagiri, *ACS Catal.*, 2016, **6**, 219–229.
19 X. Yan, C. Chen, Y. Wu, S. Liu, Y. Chen, R. Feng, J. Zhang and B. Han, *Chem. Sci.*, 2021, **12**, 6638–6645.
20 C. Choi, T. Cheng, M. Flores Espinosa, H. Fei, X. Duan, W. A. Goddard 3rd and Y. Huang, *Adv. Mater.*, 2019, **31**, 1805405.
21 T. Adit Maark and B. R. K. Nanda, *J. Phys. Chem. C*, 2017, **121**, 4496–4504.
22 E. L. Clark, C. Hahn, T. F. Jaramillo and A. T. Bell, *J. Am. Chem. Soc.*, 2017, **139**, 15848–15857.
23 D. Ren, B. S.-H. Ang and B. S. Yeo, *ACS Catal.*, 2016, **6**, 8239–8247.
24 S. B. Varandili, D. Stoian, J. Vavra, K. Rossi, J. R. Pankhurst, Y. T. Guntern, N. López and R. Buonsanti, *Chem. Sci.*, 2021, **12**, 14484–14493.
25 X. Wang, Z. Wang, T. Zhuang, C.-T. Dinh, J. Li, D.-H. Nam, F. Li, C.-W. Huang, C.-S. Tan, Z. Chen, M. Chi, C. M. Gabardo, A. Seifitokaldani, P. Todorović, A. Proppe, Y. Pang, A. R. Kirmani, Y. Wang, A. H. Ip, L. J. Richter, B. Scheffel, A. Xu, S.-C. Lo, S. O. Kelley, D. Sinton and E. H. Sargent, *Nat. Commun.*, 2019, **10**, 5186.
26 Y. C. Li, Z. Wang, T. Yuan, D. H. Nam, M. Luo, J. Wicks, B. Chen, J. Li, F. Li, F. Pelayo García de Arquer, Y. Wang, C. T. Dinh, O. Voznyy, D. Sinton and E. H. Sargent, *J. Am. Chem. Soc.*, 2019, **141**, 8584–8591.
27 X. Wang, P. Ou, J. Wicks, Y. Xie, Y. Wang, J. Li, J. Tam, D. Ren, J. Y. Howe, Z. Wang, A. Ozden, Y. Z. Finfrock, Y. Xu, Y. Li, A. S. Rasouli, K. Bertens, A. H. Ip, M. Graetzel, D. Sinton and E. H. Sargent, *Nat. Commun.*, 2021, **12**, 3387.
28 Y. Chen, Z. Fan, J. Wang, C. Ling, W. Niu, Z. Huang, G. Liu, B. Chen, Z. Lai, X. Liu, B. Li, Y. Zong, L. Gu, J. Wang, X. Wang and H. Zhang, *J. Am. Chem. Soc.*, 2020, **142**, 12760–12766.
29 T. T. H. Hoang, S. Verma, S. Ma, T. T. Fister, J. Timoshenko, A. I. Frenkel, P. J. A. Kenis and A. A. Gewirth, *J. Am. Chem. Soc.*, 2018, **140**, 5791–5797.
30 J. Huang, M. Mensi, E. Oveisi, V. Mantella and R. Buonsanti, *J. Am. Chem. Soc.*, 2019, **141**, 2490–2499.
31 J. Gao, D. Ren, X. Guo, S. M. Zakeeruddin and M. Gratzel, *Faraday Discuss.*, 2019, **215**, 282–296.
32 J. Gao, H. Zhang, X. Guo, J. Luo, S. M. Zakeeruddin, D. Ren and M. Gratzel, *J. Am. Chem. Soc.*, 2019, **141**, 18704–18714.
33 Y. Chen, Z. Fan, J. Wang, C. Ling, W. Niu, Z. Huang, G. Liu, B. Chen, Z. Lai, X. Liu, B. Li, Y. Zong, L. Gu, J. Wang, X. Wang and H. Zhang, *J. Am. Chem. Soc.*, 2020, **142**, 12760–12766.
34 R. Feng, Q. Zhu, M. Chu, S. Jia, J. Zhai, H. Wu, P. Wu and B. Han, *Green Chem.*, 2020, **22**, 7560–7565.
35 L. Hou, J. Han, C. Wang, Y. Zhang, Y. Wang, Z. Bai, Y. Gu, Y. Gao and X. Yan, *Inorg. Chem. Front.*, 2020, **7**, 2097–2106.
36 L. Xiong, X. Zhang, H. Yuan, J. Wang, X. Yuan, Y. Lian, H. Jin, H. Sun, Z. Deng, D. Wang, J. Hu, H. Hu, J. Choi, J. Li, Y. Chen, J. Zhong, J. Guo, M. H. Rummerli, L. Xu and Y. Peng, *Angew. Chem., Int. Ed.*, 2021, **60**, 2508–2518.
37 X. Wang, P. Ou, A. Ozden, S. Hung, J. Tam, C. M. Gabardo, J. Y. Howe, J. Sisler, K. Bertens, F. P. García de Arquer, R. K. Miao, C. P. O'Brien, Z. Wang, J. Abed, A. S. Rasouli, M. Sun, A. H. Ip, D. Sinton and E. H. Sargent, *Nat. Energy*, 2022, **7**, 170–176.
38 L. R. L. Ting, R. García-Muelas, A. J. Martín, F. L. P. Veenstra, S. T.-J. Chen, Y. Peng, E. Y. X. Per, S. Pablo-García, N. López, J. Pérez-Ramírez and B. S. Yeo, *Angew. Chem., Int. Ed.*, 2020, **59**, 21072.
39 H. S. Jeon, S. Kunze, F. Scholten and B. Roldan Cuenya, *ACS Catal.*, 2018, **8**, 531.
40 A. Beniya and S. Higashi, *Nat. Catal.*, 2019, **2**, 590–602.
41 Y. Zhou, F. Che, M. Liu, C. Zou, Z. Liang, P. D. Luna, H. Yuan, J. Li, Z. Wang, H. Xie, H. Li, P. Chen, E. Bladt, R. Quintero-Bermudez, T.-K. Sham, S. Bals, J. Hofkens, D. Sinton, G. Chen and E. H. Sargent, *Nat. Chem.*, 2018, **10**, 974–980.
42 Y. Huang, C. W. Ong and B. S. Yeo, *ChemSusChem*, 2018, **11**, 3299.
43 B. Roldan Cuenya, F. Scholten, K. C. Nguyen, J. P. Bruce and M. Heyde, *Angew. Chem., Int. Ed.*, 2021, **60**, 19169–19175.
44 S. Ma, M. Sadakiyo, M. Heima, R. Luo, R. T. Haasch, J. I. Gold, M. Yamauchi and P. J. A. Kenis, *J. Am. Chem. Soc.*, 2017, **139**, 47–50.
45 W. Guo, S. Liu, X. Tan, R. Wu, X. Yan, C. Chen, Q. Zhu, L. Zheng, J. Ma, J. Zhang, Y. Huang, X. Sun and B. Han, *Angew. Chem., Int. Ed.*, 2021, **60**, 21979–21987.
46 J. Wang, C. Cheng, B. Huang, J. Cao, L. Li, Q. Shao, L. Zhang and X. Huang, *Nano Lett.*, 2021, **21**, 980–987.
47 Z. Zeng, L. Y. Gan, H. Bin Yang, X. Su, J. Gao, W. Liu, H. Matsumoto, J. Gong, J. Zhang, W. Cai, Z. Zhang, Y. Yan, B. Liu and P. Chen, *Nat. Commun.*, 2021, **12**, 4088.
48 M. Li, B. Hua, L.-C. Wang, J. D. Sugar, W. Wu, Y. Ding, J. Li and D. Ding, *Nat. Catal.*, 2021, **4**, 274–283.
49 H.-Q. Liang, S. Zhao, X.-M. Hu, M. Ceccato, T. Skrydstrup and K. Daasbjerg, *ACS Catal.*, 2021, **11**, 958–966.
50 X. Feng, K. Jiang, S. Fan and M. W. Kanan, *ACS Cent. Sci.*, 2016, **2**, 169–174.
51 A. Verdaguer-Casadevall, C. W. Li, T. P. Johansson, S. B. Scott, J. T. McKeown, M. Kumar, I. E. Stephens, M. W. Kanan and I. Chorkendorff, *J. Am. Chem. Soc.*, 2015, **137**, 9808–9811.
52 X. Wang, K. Klingan, M. Klingenhof, T. Moller, J. Ferreira de Araujo, I. Martens, A. Bagger, S. Jiang, J. Rossmeisl, H. Dau and P. Strasser, *Nat. Commun.*, 2021, **12**, 794.
53 K. J. P. Schouten, Z. Qin, E. P. Gallent and M. T. M. Koper, *J. Am. Chem. Soc.*, 2012, **134**, 9864–9867.
54 Z. Zhang, G. Wen, D. Luo, B. Ren, Y. Zhu, R. Gao, H. Dou, G. Sun, M. Feng, Z. Bai, A. Yu and Z. Chen, *J. Am. Chem. Soc.*, 2021, **143**, 6855–6864.
55 J. Y. Kim, D. Hong, J. C. Lee, H. G. Kim, S. Lee, S. Shin, B. Kim, H. Lee, M. Kim, J. Oh, G. D. Lee, D. H. Nam and Y. C. Joo, *Nat. Commun.*, 2021, **12**, 3765.
56 S. Ma, M. Sadakiyo, M. Heima, R. Luo, R. T. Haasch, J. I. Gold, M. Yamauchi and P. J. A. Kenis, *J. Am. Chem. Soc.*, 2017, **139**, 47–50.
57 W. Ren, X. Tan, J. Qu, S. Li, J. Li, X. Liu, S. P. Ringer, J. M. Cairney, K. Wang, S. C. Smith and C. Zhao, *Nat. Commun.*, 2021, **12**, 1449.